Black hole critical behavior with the generalized BSSN formulation

Arman Akbarian[1] and Matthew W. Choptuik[2]

[1]*Department of Physics and Astronomy, University of British Columbia, Vancouver, British Columbia V6T 1Z1, Canada*
[2]*CIFAR Cosmology and Gravity Program Department of Physics and Astronomy, University of British Columbia, Vancouver, British Columbia V6T 1Z1, Canada*

The development of hyperbolic formulations of Einstein's equations has revolutionized our ability to perform long-time, stable, accurate numerical simulations of strong field gravitational phenomena. However, hyperbolic methods have seen relatively little application in one area of interest, type II critical collapse, where the challenges for a numerical code are particularly severe. Using the critical collapse of a massless scalar field in spherical symmetry as a test case, we study a generalization of the Baumgarte-Shapiro-Shibata-Nakamura formulation due to Brown that is suited for use with curvilinear coordinates. We adopt standard dynamical gauge choices, including 1+log slicing and a shift that is either zero or evolved by a Gamma-driver condition. With both choices of shift we are able to evolve sufficiently close to the black hole threshold to (1) unambiguously identify the discrete self-similarity of the critical solution, (2) determine an echoing exponent consistent with previous calculations, and (3) measure a mass scaling exponent, also in accord with prior computations. Our results can be viewed as an encouraging first step towards the use of hyperbolic formulations in more generic type II scenarios, including the as yet unresolved problem of critical collapse of axisymmetric gravitational waves.

I. INTRODUCTION

In this paper we investigate the application of the Baumgarte-Shapiro-Shibata-Nakamura (BSSN) formulation of Einstein's equations [1,2], as well as the dynamical coordinate choices typically associated with it, within the context of critical gravitational collapse. The BSSN formulation is a recasting of the standard $3 + 1$ Arnowitt-Deser-Misner (ADM) [3] equations that is known to be strongly hyperbolic [4,5] and suitable for numerical studies. It has been widely used in numerical relativity and provides a robust and stable evolution for the spacetime geometry. Most notably, various implementations of this formulation have allowed successful computation of dynamical spacetimes describing binaries of gravitationally compact objects [6–8]. The standard gauge choices in BSSN—namely the $1 + \log$ slicing condition [9] and the Gamma-driver shift condition [10]—are partial differential equations (PDEs) of evolutionary type. Furthermore, the BSSN approach results in a set of so-called free evolution equations, meaning that the Hamiltonian and momentum constraints are only solved at the initial time. Thus, once initial data have been determined, one only has to solve time-dependent PDEs in order to compute the geometric variables in the BSSN scheme. In particular, during the evolution there is no need to solve any elliptic equations, which in general could arise either from the constraints or from coordinate conditions. This is advantageous since it can be quite challenging to implement efficient numerical elliptic solvers.

In addition to the BSSN approach, the numerical relativity community has adopted the generalized harmonic (GH) [11] formulation of Einstein's equations, which is also strongly hyperbolic and has performed very well in simulations of compact binaries [8,12]. Like BSSN, the GH formulation is of evolutionary type so that all of the metric components satisfy time-dependent PDEs. It too uses dynamical coordinate choices: in this case one needs to provide a prescription for the evolution of the harmonic functions defined by $H^\mu \equiv \Box x^\mu$.

Despite the tremendous success of these hyperbolic formulations in evolving strongly gravitating spacetimes containing black holes and neutron stars, they have not seen widespread use in another area of strong gravity physics typically studied via numerical relativity, namely critical phenomena in gravitational collapse. First reported in [13] and briefly reviewed below, critical phenomena emerge at the threshold of black hole formation and present significant challenges for thorough and accurate computational treatment. The original observation of critical behavior as well as many of the subsequent studies were restricted to spherical symmetry (for a review, see [14,15]) and there is a clear need to extend the work to more generic cases. In this respect the BSSN and GH formulations would appear to be attractive frameworks. However, it is not yet clear if these hyperbolic formulations, in conjunction with the standard dynamical gauge choices that have been developed, will allow the critical regime to be probed without the development of coordinate pathologies. Particularly notable in this regard is an implementation of the GH formulation that was

employed by Sorkin and Choptuik [16] to study the critical collapse of a massless scalar field in spherical symmetry. Despite extensive experimentation with a variety of coordinate conditions, the code that was developed was not able to calculate near-critical spacetimes: coordinate singularities invariably formed once the critical regime was approached. A natural question that then arises is whether the BSSN formulation (including the standard dynamical gauge choices used with it) is similarly problematic or if it provides an effective framework to study critical phenomena.

Here we begin the task of addressing this question by revisiting the model of spherically symmetric massless scalar collapse. We use a generalization of the BSSN formulation due to Brown [17] that is well suited for use with curvilinear coordinates. The choice of a massless scalar field as the matter source has the great advantage that the nature of the critical solution is very well known [18–23], making it straightforward for us to determine if and when our approach has been successful. We note that although the calculations described below *are* restricted to spherical symmetry our ultimate goal is to develop an evolutionary scheme—including gauge choices—that can be applied to a variety of critical phenomena studies in axial symmetry and ultimately generic cases.

We now briefly review the main concepts and features of black hole critical phenomena that are most pertinent to the work in this paper. Full details and pointers to the extensive literature on the subject may be found in review articles [14,15].

Critical phenomena in gravitational collapse can be described as a phase transition, analogous to that in a thermodynamic system. Under certain assumptions, a matter source coupled to the Einstein gravitational field will evolve to one of two distinct final phases. On the one hand, weak initial data will eventually disperse to infinity leaving flat spacetime as the end state. On the other hand, sufficiently strong data will develop significant self gravitation and then collapse, resulting in a final phase which contains a black hole. Quite generically, remarkable behavior emerges at and near the transition between these phases, and this behavior is precisely what we mean by the critical phenomena in the system under consideration.

It transpires that there are two broad classes of critical phenomena that can be distinguished by the behavior of the black hole mass at threshold. The class of interest here, known as type II, is characterized by infinitesimal mass at the transition. Further, the black hole mass, M_{BH}, satisfies a scaling law:

$$M_{BH} \sim |p - p^\star|^\gamma, \qquad (1)$$

where p is an arbitrary parameter that controls the strength of the matter source at the initial time, $p^\star$ is the parameter value at threshold and the mass scaling exponent, γ, is a

constant that is independent of the choice of the initial data. Type II behavior is also characterized by the emergence of a unique solution at threshold which is generically self-similar. In some cases, including the massless scalar field, the self-similarity is discrete. Specifically, in spherically symmetric critical collapse with discrete self-similarity (DSS), as $p \to p^\star$ we find

$$Z^\star(\rho + \Delta, \tau + \Delta) \sim Z^\star(\rho, \tau), \qquad (2)$$

where $Z^\star$ represents some scale-invariant component (function) of the critical solution. Here $\rho \equiv \ln(r_S)$ and $\tau \equiv \ln(T_S - T_S^\star)$ are logarithmically rescaled values of the areal radius, r_S, and polar time, T_S, respectively, and $T_S^\star$ is the accumulation time at which the central singularity associated with the DSS solution forms. T_S has been normalized so that it measures proper time at the origin. As with γ, the echoing (rescaling) exponent, Δ, is a universal constant for a specific matter source; i.e. it is independent of the form of the initial data.

Another feature of type II collapse, intimately related to the self-similarity of the critical solution, is that the curvature can become arbitrarily large: in the limit of infinite fine-tuning, $p \to p^\star$, a naked singularity forms. Furthermore, the echoing behavior (2) results in the development of fine structure in the solution around the center of the scaling symmetry. Observing this structure and measuring the echoing exponent Δ associated with it requires a code that can reliably evolve solutions very close to the critical spacetime and that provides sufficient numerical resolution in the vicinity of the accumulation point $(r_S, T_S) = (0, T_S^\star)$.

As mentioned above, most studies of critical phenomena have assumed spherical symmetry. This is particularly so for the case of type II behavior where the resolution demands dictated by the self-similarity of the critical solutions make multidimensional work extremely computationally intensive. As far as we know, the only work in spherical symmetry to have used a purely evolutionary approach based on the BSSN or GH forms of the Einstein equations is [16] which, as we have noted, was not successful in isolating the critical solution.[1] In axisymmetry there have been two investigations of type II collapse of massless scalar fields [25,26], and several of type II collapse of pure gravitational waves (vacuum) [27–31]. Of these, only Alcubierre *et al.*'s [28] and Sorkin's [31] calculations of vacuum collapse adopted hyperbolic formalisms, and only the scalar field calculations—which employed a modified ADM formulation and partially constrained evolution—were able to completely resolve the critical behavior, including the discrete self-similarity of

---

[1]However, see [24] for an investigation of type II behavior in the collapse of a scalar field in $2 + 1$ anti–de Sitter spacetime that employs an *ad hoc* free evolution scheme.

the critical solutions. In the fully three-space dimension (3D) context there have also been a few studies of type II collapse to date. Perhaps most notable is the recent work of Healy and Laguna [32] which used a massless scalar field as a matter source and the BSSN formulation with standard dynamical gauge choices. The authors were able to observe the mass scaling (1) with a measured $\gamma \approx 0.37$ consistent with calculations in spherical symmetry. However, they were not able to conclusively see the discrete self-similarity of the critical solution; in particular they could not accurately measure the echoing exponent, Δ. This shortcoming was attributed to a lack of computational resources rather than a breakdown of the underlying methodology, including the coordinate conditions that were adopted. Finally, there have been two attempts to probe the black hole threshold for the collapse of pure gravitational waves in 3D [33,34]. Both employed a BSSN approach with, for the most part, standard dynamical gauge choices. In both cases problems with the gauge apparently precluded calculation near the critical point (although resolution limitations may also have been an issue) and neither the mass scaling nor the echoing exponent could be estimated in either study.

We can thus summarize the state of the art in the use of hyperbolic formulations for the study of type II critical collapse as follows: to our knowledge there has been no implementation of a fully evolutionary scheme, based on either BSSN or GH, that has allowed for evolution sufficiently close to a precisely critical solution to allow the unambiguous identification of discrete self-similarity (or continuous self-symmetry for that matter). Again, and particularly in light of the experience of [16], the key aim of this paper is to investigate the extent to which it *is* possible to use a BSSN scheme to fully resolve type II solutions. A major concern here is the appropriate choice of coordinate conditions, not least since dynamical gauge choices can be prone to the development of gauge shocks and other types of coordinate singularities [35,36]. Such pathologies could, in principle, prevent a numerical solver from evolving the spacetime in or near the critical regime.

Now, as Garfinkle and Gundlach have discussed in detail [37], an ideal coordinate system for numerical studies of type II collapse is one which *adapts* itself to the self-similarity: for the DSS case this means that the metric coefficients and relevant matter variables are exactly periodic in the coordinates in the fashion given by (2). Clearly, if the coordinate system *is* adapted, then other than at the naked singularity—which is inaccessible via finite-precision calculations—it should remain nonsingular during a numerical evolution. One can then argue that ensuring that the numerical scheme has adequate resolution will be the key to successful simulation of the critical behavior. At the same time, it is also clear that there will be coordinate systems which do not necessarily adapt but which nonetheless remain nonsingular during critical collapse, at least

over some range of scales, and which are therefore potentially useful for numerical calculations. We will see below that there is strong evidence that the coordinate systems we have used belong to the latter class, and weaker evidence that they *do* adapt to the self-similarity.

Another potential source of problems, which is not specific to hyperbolic formulations, relates to our restriction to spherical symmetry. As is well known, the singular points of curvilinear coordinate systems, $r = 0$ in our case, can sometimes require special treatment to ensure that numerical solutions remain regular there. In critical collapse the highly dynamical nature of the solution near $r = 0$ might naturally be expected to exacerbate problems with regularity. In the work described below we have paid special attention to the ability of our approach to both fully resolve the near-critical configuration and maintain regularity of the solution at the origin.

The remainder of this paper is organized as follows: in Sec. II we review the generalized BSSN formulation and display the equations of motion for our model system. Section III expands the discussion of the issue of regularity at the coordinate singularity point, describes the numerical approach we have adopted, and provides details concerning the various tests and diagnostics we have used to validate our implementation. In Sec. IV we present results computed using two distinct choices for the shift vector and provide conclusive evidence that the generalized BSSN formulation is capable of evolving in the critical regime in both cases. Section V contains some brief concluding remarks, and further details concerning the BSSN formalism in spherical symmetry and the scalar field equations of motion are included in Appendixes A and B, respectively. We adopt units where the gravitational constant and the speed of light are both unity: $G = c = 1$.

II. EQUATIONS OF MOTION

The dynamical system we intend to study in the critical collapse regime is a real, massless scalar field, Ψ, self gravitating via Einstein's equations,

$$G_{\mu\nu} = 8\pi T_{\mu\nu}. \tag{3}$$

Here, $T_{\mu\nu}$ is the energy-momentum tensor associated with the minimally coupled Ψ:

$$T_{\mu\nu} = \nabla_\mu \nabla_\nu \Psi - \frac{1}{2} g_{\mu\nu} \nabla^\eta \Psi \nabla_\eta \Psi, \tag{4}$$

and the evolution of the scalar field is given by

$$\nabla^\mu \nabla_\mu \Psi = 0. \tag{5}$$

The time development of the geometry is then given by recasting Einstein's equations as an evolution system based on the usual $3 + 1$ expression for the spacetime metric:

$$ds^2 = -\alpha^2 dt^2 + \gamma_{ij}(dx^i + \beta^i dt)(dx^j + \beta^j dt). \quad (6)$$

Here, the 3-metric components, γ_{ij}, are viewed as the fundamental dynamical geometrical variables and the lapse function, α, and shift vector, β^i, which encode the coordinate freedom of general relativity, must in general be prescribed independently of the equations of motion.

A. Generalized BSSN

We now summarize the BSSN formulation of Einstein's equations and describe how it can be adapted to curvilinear coordinates. Readers interested in additional details are directed to [38] for a more pedagogical discussion.

In the standard ADM formulation [3,39], the dynamical Einstein equations are rewritten as evolution equations for the 3-metric and the extrinsic curvature $\{\gamma_{ij}, K_{ij}\}$. The first difference between the BSSN formulation and the ADM decomposition is the conformal rescaling of the ADM dynamical variables:

$$\gamma_{ij} = e^{4\phi}\tilde{\gamma}_{ij}, \quad (7)$$

$$K_{ij} = e^{4\phi}\tilde{A}_{ij} + \frac{1}{3}\gamma_{ij}K, \quad (8)$$

where e^{ϕ} is the conformal factor, $\tilde{\gamma}_{ij}$ is the conformal metric, $\tilde{A}_{ij}$ is the conformally rescaled trace-free part of the extrinsic curvature and $K = \gamma^{ij}K_{ij}$ is the trace of the extrinsic curvature. Here by fixing the trace of $\tilde{A}_{ij}$, and the determinant of the conformal metric, the set of primary ADM dynamical variables transforms to the new set:

$$\{\gamma_{ij}, K_{ij}\} \rightarrow \{\phi, \tilde{\gamma}_{ij}, K, \tilde{A}_{ij}\}, \quad (9)$$

in the BSSN formulation.

In the original BSSN approach, the conformal metric $\tilde{\gamma}_{ij}$ is taken to have determinant $\tilde{\gamma} = 1$. However this choice is only suitable when we adopt coordinates in which the determinant of the flat-space metric reduces to unity. This is the case, of course, for Cartesian coordinates but is not so for general curvilinear systems. For instance, the flat 3-metric in spherical coordinates,

$$ds^2 = dr^2 + r^2 d\theta^2 + r^2\sin^2\theta d\phi^2, \quad (10)$$

has determinant $\overset{\circ}{\gamma} = r^4\sin^2\theta$. Recently, Brown [17] has resolved this issue by introducing a covariant version of the BSSN equations—the so-called *generalized* BSSN formulation, which we hereafter refer to as G-BSSN—in which the primary dynamical variables are tensors so that the formulation can be adapted to non-Cartesian coordinate systems. In G-BSSN we no longer assume that the conformal 3-metric has determinant one. Rather, ϕ becomes a true scalar and for its dynamics to be determined

a prescription for the time evolution of the determinant of $\tilde{\gamma}_{ij}$ must be given. In the following this will be done by requiring that the determinant be constant in time.

Another main difference between the ADM decomposition and BSSN is that the mixed spatial derivative terms occurring in the 3-Ricci tensor are eliminated through the definition of a new quantity, $\tilde{\Gamma}^k$:

$$\tilde{\Gamma}^k \equiv \tilde{\gamma}^{ij}\tilde{\Gamma}^k_{ij}, \quad (11)$$

which becomes an additional, independent dynamical variable. Note that $\tilde{\Gamma}^i$ is not a vector as it is coordinate dependent. To extend this redefinition so that it is well suited for all coordinate choices, in G-BSSN we define

$$\tilde{\Lambda}^k \equiv \tilde{\gamma}^{ij}(\tilde{\Gamma}^k_{ij} - \overset{\circ}{\Gamma}{}^k_{ij}) = \tilde{\Gamma}^k - \overset{\circ}{\Gamma}{}^k_{ij}\tilde{\gamma}^{ij}, \quad (12)$$

where $\overset{\circ}{\Gamma}{}^k_{ij}$ denotes the Christoffel symbols associated with the flat metric. This definition makes this so-called conformal connection, $\tilde{\Lambda}^i$, a true vector and it becomes a primary dynamical variable in G-BSSN.

We now summarize the G-BSSN equations, referring the reader to [40] for more details, including a full derivation. We begin by defining $\partial_\perp$, the time derivative operator acting normally to the $t = $ const. slices:

$$\partial_\perp \equiv \partial_t - \mathcal{L}_{\vec{\beta}}, \quad (13)$$

where $\mathcal{L}_{\vec{\beta}}$ denotes the Lie derivative along $\vec{\beta}$. We then have

$$\partial_\perp\phi = -\frac{1}{6}\alpha K + \sigma\frac{1}{6}\tilde{D}_k\beta^k, \quad (14)$$

$$\partial_\perp\tilde{\gamma}_{ij} = -2\alpha\tilde{A}_{ij} - \sigma\frac{2}{3}\tilde{A}_{ij}\tilde{D}_k\beta^k, \quad (15)$$

$$\partial_\perp K = -\gamma^{ij}D_jD_i\alpha + \alpha\left(\tilde{A}_{ij}\tilde{A}^{ij} + \frac{1}{3}K^2\right) + 4\pi(\rho + S), \quad (16)$$

$$\partial_\perp\tilde{A}_{ij} = e^{-4\phi}[-D_iD_j\alpha + \alpha(R_{ij} - 8\pi S_{ij})]^{\mathrm{TF}}$$
$$+ \alpha(K\tilde{A}_{ij} - 2\tilde{A}_{il}\tilde{A}^l{}_j) - \sigma\frac{2}{3}\tilde{A}_{ij}\tilde{D}_k\beta^k, \quad (17)$$

$$\partial_\perp\tilde{\Gamma}^i = -2\tilde{A}^{ij}\partial_j\alpha + \tilde{\gamma}^{lj}\partial_j\partial_l\beta^i$$
$$+ 2\alpha\left(\tilde{\Gamma}^i_{jk}\tilde{A}^{kj} - \frac{2}{3}\tilde{\gamma}^{ij}\partial_jK + 6\tilde{A}^{ij}\partial_j\phi - 8\pi\tilde{\gamma}^{ij}S_j\right)$$
$$+ \frac{\sigma}{3}[2\tilde{\Gamma}^i\tilde{D}_k\beta^k + \tilde{\gamma}^{li}\partial_l(\tilde{D}_k\beta^k)]. \quad (18)$$

Here, a superscript TF denotes the trace-free part (with respect to the 3-metric γ_{ij}) of a tensor, and $\tilde{D}_i$ is the

covariant derivative associated with the conformal metric $\tilde{\gamma}_{ij}$. Additionally, the quantity σ is an adjustable parameter that is discussed below and typically is either 0 or 1. Note that all the Lie derivatives in the G-BSSN equations operate on true tensors and vectors of weight 0. For instance,

$$\mathcal{L}_{\vec{\beta}}\tilde{A}_{ij} = \beta^k\partial_k\tilde{A}_{ij} + \tilde{A}_{ik}\partial_j\beta^k + \tilde{A}_{kj}\partial_i\beta^k. \quad (19)$$

Furthermore, in G-BSSN, rather than evolving (18), the redefined conformal connection, $\tilde{\Lambda}^i$, is evolved via

$$\partial_t\tilde{\Lambda}^k = \partial_t\tilde{\Gamma}^k - \overset{\circ}{\Gamma}{}^k_{ij}\partial_t\tilde{\gamma}^{ij}, \quad (20)$$

where the time derivative $\partial_t\tilde{\gamma}^{ij}$ is eliminated using (15). In Eq. (17), R_{ij} denotes the 3-Ricci tensor associated with γ_{ij} and can be written as the sum

$$R_{ij} = R^\phi_{ij} + \tilde{R}_{ij}, \quad (21)$$

where R^ϕ_{ij} is given by

$$R^\phi_{ij} = -2\tilde{D}_i\tilde{D}_j\phi - 2\tilde{\gamma}_{ij}\tilde{D}^k\tilde{D}_k\phi + 4\tilde{D}_i\phi\tilde{D}_j\phi - 4\tilde{\gamma}_{ij}\tilde{D}^k\phi\tilde{D}_k\phi, \quad (22)$$

and $\tilde{R}_{ij}$ is the 3-Ricci tensor associated with the conformal metric:

$$\tilde{R}_{ij} = -\frac{1}{2}\tilde{\gamma}^{lm}\partial_m\partial_l\tilde{\gamma}_{ij} + \tilde{\gamma}_{k(i}\partial_{j)}\tilde{\Gamma}^k + \tilde{\Gamma}^k\tilde{\Gamma}_{(ij)k} \\ + \tilde{\gamma}^{lm}(2\tilde{\Gamma}^k_{l(i}\tilde{\Gamma}_{j)km} + \tilde{\Gamma}^k_{im}\tilde{\Gamma}_{klj}). \quad (23)$$

The matter fields ρ, S, S_i and S_{ij} are defined by

$$\rho = n_\mu n_\nu T^{\mu\nu}, \quad (24)$$

$$S = \gamma^{ij}S_{ij}, \quad (25)$$

$$S^i = -\gamma^{ij}n^\mu T_{\mu j}, \quad (26)$$

$$S_{ij} = \gamma_{i\mu}\gamma_{i\nu}T^{\mu\nu}, \quad (27)$$

where n^μ is the unit normal vector to the $t = \text{const}$ slices.

As mentioned previously, we need to prescribe dynamics for the determinant of $\tilde{\gamma}_{ij}$ to have a complete set of equations of motion for the G-BSSN dynamical variables. One approach is to fix the determinant to its initial value by demanding that

$$\partial_t\tilde{\gamma} = 0. \quad (28)$$

This is the so-called Lagrangian option and is associated with the choice $\sigma = 1$ in the equations. Another option is to define the determinant to be constant along the normal

direction to the time slices, which can be implemented by requiring $\partial_\perp\tilde{\gamma} = 0$. This is usually referred to as the Lorentzian option, and is associated with the choice $\sigma = 0$. Here we choose (28), i.e. $\sigma = 1$.

Note that in the G-BSSN equations the divergence of the shift vector,

$$\tilde{D}_k\beta^k = \frac{1}{\sqrt{\tilde{\gamma}}}\partial_k(\sqrt{\tilde{\gamma}}\beta^k), \quad (29)$$

no longer reduces to $\partial_k\beta^k$ since the determinant of the conformal metric $\tilde{\gamma}_{ij}$ is not necessarily 1, but by virtue of the choice (28) is equal to that of the initial background flat metric in the chosen curvilinear coordinates.

As usual, when setting initial data for any given evolution of the coupled Einstein-matter equations we must solve the Hamiltonian and momentum constraints. In terms of the G-BSSN variables these are

$$\mathcal{H} \equiv \tilde{\gamma}^{ij}\tilde{D}_i\tilde{D}_j e^\phi - \frac{e^\phi}{8}\tilde{R} + \frac{e^{5\phi}}{8}\tilde{A}^{ij}\tilde{A}_{ij} \\ - \frac{e^{5\phi}}{12}K^2 + 2\pi e^{5\phi}\rho = 0, \quad (30)$$

$$\mathcal{M}^i \equiv \tilde{D}_j(e^{6\phi}\tilde{A}^{ji}) - \frac{2}{3}e^{6\phi}\tilde{D}^iK - 8\pi e^{6\phi}S^i = 0. \quad (31)$$

B. G-BSSN in spherical symmetry and gauge choices

In spherical symmetry a generic form of the conformal metric $\tilde{\gamma}_{ij}$ is given by

$$\tilde{\gamma}_{ij} = \begin{pmatrix} \tilde{\gamma}_{rr}(t,r) & 0 & 0 \\ 0 & r^2\tilde{\gamma}_{\theta\theta}(t,r) & 0 \\ 0 & 0 & r^2\tilde{\gamma}_{\theta\theta}(t,r)\sin^2\theta \end{pmatrix}. \quad (32)$$

Similarly, a suitable *ansatz* for the traceless extrinsic curvature is

$$\tilde{A}_{ij} = \begin{pmatrix} \tilde{A}_{rr}(t,r) & 0 & 0 \\ 0 & r^2\tilde{A}_{\theta\theta}(t,r) & 0 \\ 0 & 0 & r^2\tilde{A}_{\theta\theta}(t,r)\sin^2\theta \end{pmatrix}. \quad (33)$$

The shift vector and $\tilde{\Lambda}^i$ have only radial components:

$$\beta^i = [\beta(t,r),0,0], \quad (34)$$

$$\tilde{\Lambda}^i = [\tilde{\Lambda}(t,r),0,0]. \quad (35)$$

Given (32)–(35), the G-BSSN equations become a set of first order evolution equations for the seven primary variables

$$\{\phi(t, r), \tilde{\gamma}_{rr}(t, r), \tilde{\gamma}_{\theta\theta}(t, r), K(t, r),$$
$$\tilde{A}_{rr}(t, r), \tilde{A}_{\theta\theta}(t, r), \tilde{\Lambda}(t, r)\}.$$

These are coupled to the evolution equation (5) for the scalar field and constrained by the initial conditions (30)–(31). The explicit expressions for the full set of equations of motion are given in Appendix A.

To fix the time slicing we implement a nonadvective[2] version of the $1 + \log$ slicing condition[3]:

$$\partial_t \alpha = -2\alpha k. \tag{36}$$

For the spatial coordinates we either choose a zero shift,

$$\beta^i = 0, \tag{37}$$

or use what we will term the Gamma-driver condition:

$$\partial_t \beta^i = \mu \tilde{\Lambda}^i - \eta \beta^i. \tag{38}$$

Here, μ and η are adjustable parameters which we set to $\mu = 3/4$ and $\eta \simeq 1/(2M_{\text{ADM}})$, where M_{ADM} is the total mass of the system measured at infinity (see Sec. III D 1). We emphasize that (38) is *not* the usual Gamma-driver equation used in the standard BSSN approach,

$$\partial_t \beta^i = \mu \tilde{\gamma}^i - \eta \beta^i, \tag{39}$$

but since it is a natural extension of the above to the G-BSSN case we have opted to use the same nomenclature. In the rest of this paper, we frequently refer to the shift vector evolved via (38) as β^G. Explicitly, in spherical symmetry β^G is defined by

$$\partial_t \beta^G(t, r) = \mu \tilde{\Lambda}(t, r) - \eta \beta^G(t, r). \tag{40}$$

III. NUMERICS

We use a second order finite differencing method to discretize Eqs. (14)–(17) and (20). Further, the equations of motion are transformed to a compactified radial coordinate that we denote by $\tilde{r}$ and which is defined in terms of the original coordinate r by

---

[2]The terminology *nonadvective* derives from the absence of an advective term, $\beta^j \partial_j$, on the left-hand side of Eqs. (36) and (38). We note that we also experimented with the advective versions of the equations. The results were very similar to those for the nonadvective case; in particular, near-critical solutions exhibiting echoing and scaling could also be obtained.

[3]The reader can easily check that in the case of zero shift, the lapse choice given by (36) combined with (14) implies $\partial_t(\alpha - \phi/12) = 0$. In Cartesian coordinates $\phi/12 \equiv \ln \gamma$, so this last equation gives $\alpha - \ln \gamma = c(\vec{x})$, where the function $c(\vec{x})$ is time independent. The choice $c(\vec{x}) = 1$ then yields an algebraic expression for the lapse, $\alpha = 1 + \ln \gamma$, which is the origin of the terminology "$1 + \log$ slicing."

$$r = e^{\tilde{r}} - e^{\delta} + \frac{R_\infty}{R_\infty - \tilde{r}} - \frac{R_\infty}{R_\infty - \delta}, \tag{41}$$

where δ and R_∞ are parameters with typical values $\delta \simeq -12$ and $R_\infty \simeq 3$. It is straightforward to verify the following: (1) the radial domain $r = (0, \infty)$ maps to the computational domain $\tilde{r} = (\delta, R_\infty)$; (2) the derivative $dr/d\tilde{r}$ decreases toward the origin ($\tilde{r} \simeq \delta$), so that a uniform grid on $\tilde{r}$ is a nonuniform grid on r with approximately 10^3 times more resolution close to the origin relative to the outer portion of the solution domain, $\tilde{r} \simeq 2$ ($r \simeq 10$), where the support of the scalar field is initially concentrated; (3) the parameter δ can be used to adjust the resolution near the origin; specifically, decreasing δ increases the resolution near $r = 0$. For notational simplicity, however, in the following we omit the explicit dependence of the fields on $\tilde{r}$ and denote the spacetime dependence of any dynamical variable X as previously: $X(t, r(\tilde{r})) \equiv X(t, r)$.

We use a finite difference grid that is uniform in $\tilde{r}$ and analytically transform all r-derivative terms in the equations of motion to their $\tilde{r}$-coordinate counterparts prior to finite differencing.

We also developed a Maple-based toolkit [41] that automates the process of discretizing an arbitrary derivative expression. This toolkit handles boundary conditions and generates a pointwise Newton-Gauss-Seidel solver in the form of Fortran routines for a given set of time-dependent or elliptic PDEs. The calculations in this paper were all carried out using this infrastructure.

A. Initialization

The matter content is set by initializing the scalar field to a localized Gaussian shell:

$$\Psi(0, r) = p \exp\left(-\frac{(r - r_0)^2}{\sigma_r^2}\right), \tag{42}$$

where p, r_0 and σ_r are parameters. Note that here r is the noncompactified radial coordinate which is related to the compactified coordinate $\tilde{r}$ via (41). A typical initial profile for the scalar field in our calculations has $\sigma_r \simeq 1$, $r_0 \simeq 10$, and p of order 10^{-1}. We use the overall amplitude factor p as the tuning parameter to find critical solutions. We initialize the conformal metric (32) to the flat metric in spherical symmetry,

$$\tilde{\gamma}_{rr}(0, r) = \tilde{\gamma}_{\theta\theta}(0, r) = 1, \tag{43}$$

and initialize the lapse function to unity,

$$\alpha(0, r) = 1. \tag{44}$$

We also demand that the initial data be time symmetric,

$$\tilde{A}_{rr}(0, r) = \tilde{A}_{\theta\theta}(0, r) = K(0, r) = 0, \tag{45}$$

$$\beta(0, r) = \tilde{\Lambda}(0, r) = 0, \qquad (46)$$

$$\partial_t \Psi(t, r)|_{t=0} = 0, \qquad (47)$$

which means that the momentum constraint (31) is trivially satisfied. This leaves the Hamiltonian constraint (30) which is solved as a two-point boundary value problem for the conformal factor at the initial time,

$$\psi(r) \equiv e^{\phi(0,r)}. \qquad (48)$$

The outer boundary condition for ψ,

$$\psi(r)|_{r=\infty} = 1, \qquad (49)$$

follows from asymptotic flatness, while at $r = 0$ we have

$$\partial_r \psi(r)|_{r=0} = 0 \qquad (50)$$

since $\psi(r)$ must be an even function in r for regularity at the origin.

B. Boundary conditions

Due to the fact that the metric has to be conformally flat at the origin we have

$$\tilde{\gamma}_{rr}(t, 0) = \tilde{\gamma}_{\theta\theta}(t, 0). \qquad (51)$$

Further, since we are using the Lagrangian choice, $\sigma = 1$, the determinant of $\tilde{\gamma}_{ij}$ must at all times be equal to its value at the initial time, so

$$\tilde{\gamma}_{rr} \tilde{\gamma}_{\theta\theta}^2 = 1. \qquad (52)$$

From these two results we have

$$\tilde{\gamma}_{rr}(t, 0) = \tilde{\gamma}_{\theta\theta}(t, 0) = 1. \qquad (53)$$

Using (53) and (15) it is then easy to see that we must also have

$$\tilde{A}_{rr}(t, 0) = \tilde{A}_{\theta\theta}(t, 0) = 0. \qquad (54)$$

As is usual when working in spherical coordinates, many of the boundary conditions that must be applied at $r = 0$ follow from the demand that the solution be regular there. Essentially, the various dynamical variables must have either even or odd "parity" with respect to expansion in r as $r \to 0$. Variables with even parity, typically scalars or diagonal components of rank-2 tensors, must have vanishing radial derivative at $r = 0$, while odd parity functions, typically radial components of vectors, will themselves vanish at the origin.

Applying these considerations to our set of unknowns we find

$$\partial_r \tilde{\gamma}_{rr}(t, r)|_{r=0} = \partial_r \tilde{\gamma}_{\theta\theta}(t, r)|_{r=0} = 0, \qquad (55)$$

$$\partial_r \tilde{A}_{rr}(t, r)|_{r=0} = \partial_r \tilde{A}_{\theta\theta}(t, r)|_{r=0} = 0, \qquad (56)$$

$$\beta(t, 0) = \tilde{\Lambda}(t, 0) = 0, \qquad (57)$$

$$\partial_r K(t, r)|_{r=0} = \partial_r \phi(t, r)|_{r=0} = \partial_r \Psi(t, r)|_{r=0} = 0. \qquad (58)$$

We use Eqs. (53)–(54) and (57) to fix the values of the functions at the origin and a forward finite differencing of (58) to update K, ϕ and Ψ at $r = 0$. Further, we apply a forward finite differencing of (55)–(56) to update the values of the function at the grid point next to the origin. The $1 + \log$ condition (36) can be used directly at $r = 0$. Again, we emphasize that all of the r-derivative terms of the boundary conditions described above are analytically transformed to the numerical coordinate, $\tilde{r}$, before the equations are finite differenced.

Since we are using compactified coordinates, all the variables are set to their flat spacetime values at the outer boundary $r = \infty$:

$$\tilde{\gamma}_{rr} = \tilde{\gamma}_{\theta\theta} = e^\phi = \alpha = 1 \quad \text{at:} \ (t, \infty), \qquad (59)$$

$$\tilde{A}_{rr} = \tilde{A}_{\theta\theta} = K = \tilde{\Lambda} = \beta = \Psi = 0 \quad \text{at:} \ (t, \infty). \qquad (60)$$

Here, we emphasize that spatial infinity, $r = \infty$, corresponds to the finite compactified (computational) coordinate point $\tilde{r} = R_\infty$.

C. Evolution scheme and regularity

We implemented a fully implicit, Crank-Nicolson [42] finite differencing scheme to evolve the system of G-BSSN equations. The precise form of the continuum equations used is given in Appendix A and all derivatives, both temporal and spatial, were approximated using second-order-accurate finite difference expressions.

During an evolution the correct limiting behavior of the spatial metric components must be maintained near $r = 0$ to ensure a regular solution. For example, the limiting values of the conformal metric components $\tilde{\gamma}_{rr}$ and $\tilde{\gamma}_{\theta\theta}$ are given by

$$\tilde{\gamma}_{rr}(t, r) = 1 + O(r^2), \qquad (61)$$

$$\tilde{\gamma}_{\theta\theta}(t, r) = 1 + O(r^2). \qquad (62)$$

If the discrete approximations of the metric functions do not satisfy these conditions, then irregularity will manifest itself in the divergence of various expressions such as the Ricci tensor component (A12)

$$R_{rr} = 2\frac{\tilde{\gamma}_{rr} - \tilde{\gamma}_{\theta\theta}}{r^2 \tilde{\gamma}_{\theta\theta}} + \cdots, \qquad (63)$$

which should converge to a finite value at the origin if conditions (61)–(62) hold.

One approach to resolve potential regularity issues is to regularize the equations [16,40,43], by redefining the primary evolution variables, so that the equations become manifestly regular at the origin. Another approach is to use implicit or partially implicit methods [44]. As recently shown by Montero and Cordeo-Carrion [45], such schemes can yield stable evolution without the need for explicit regularization. Baumgarte *et al.* [46] also adopted a similar approach—using a partially implicit scheme without regularization—in an implementation of the G-BSSN formulation in spherical polar coordinates.

As mentioned, our implementation is fully implicit and we have also found that our generalized BSSN equations can be evolved without any need for regularization at the origin, even in strong gravity scenarios where the spacetime metric has significant deviations from flatness near the origin.

That said, we also experimented with other techniques aimed at improving regularity. For example, using the constraint equation (52) and the fact that $\tilde{A}_{ij}$ is trace free,

$$\frac{\tilde{A}_{rr}}{\tilde{\gamma}_{rr}} + 2\frac{\tilde{A}_{\theta\theta}}{\tilde{\gamma}_{\theta\theta}} = 0, \qquad (64)$$

we can compute $\tilde{\gamma}_{\theta\theta}$ and $\tilde{A}_{\theta\theta}$ in terms of $\tilde{\gamma}_{rr}$ and $\tilde{A}_{rr}$, respectively, rather than evolving them. However, when we did this we found no significant improvement in regularity relative to the original scheme.

Finally, to ensure our solutions remain smooth on the scale of the mesh we use fourth order Kreiss-Oliger dissipation [47] in the numerical solution updates.

D. Tests

This section documents various tests we have made to validate the correctness of our numerical solver as well as the consistency of the finite differencing method used to evolve the system of G-BSSN equations. We use a variety of diagnostic tools, including monitoring of the constraint equations, convergence tests of the primary dynamical variables, and a direct computation to check if the metric and matter fields calculated via the G-BSSN formulation satisfy the covariant form of Einstein's equations. All of the calculations were performed using the $1 + \log$ slicing condition (36) and either $\beta = 0$ or $\beta = \beta^G$ where β^G satisfies the Gamma-driver condition (40).

1. Constraints and conserved quantities

We monitor the evolution of the constraint equations (30)–(31) during a strongly gravitating evolution where the nonlinearities of the equations are most pronounced. As demonstrated in Fig. 1(a), at resolutions
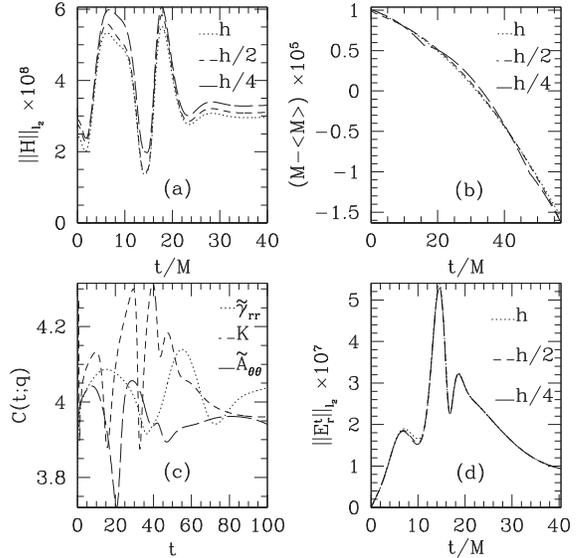

FIG. 1. Results from various tests that verify the accuracy and consistency of our numerical solver and the finite differencing method used to integrate the equations. (a) The evolution of the l_2-norm [root mean square (RMS) value] of the Hamiltonian constraint. The norm is plotted for three different resolutions h, $h/2$ and $h/4$ corresponding to $N_r = 512$, 1024 and 2048, respectively. The data for the $N_r = 1024$ and $N_r = 2048$ curves have been rescaled by factors of 4 and 16, respectively, and the overlap of the three lines thus signals the expected second order convergence to zero of the constraint deviation. We observe similar convergence properties for the momentum constraint as well as the constraint equation (12) for $\tilde{\Lambda}^i$, and the constraint (64) for the trace of $\tilde{A}_{ij}$. Additionally, since the operator used to evaluate the residual of the Hamiltonian constraint is distinct from that used in the determination of the initial data, the test also validates the initial data solver. (b) Conservation of the ADM mass during the evolution of strong initial data. Here the deviation of the mass from its time average is plotted for three different resolutions. Higher resolution values have again been rescaled so that overlap of the curves demonstrates $O(h^2)$ convergence to 0 of the deviation of the total mass. (c) The convergence factor defined in (68) for three of the primary BSSN variables: $\tilde{\gamma}_{rr}$, K, and $\tilde{A}_{\theta\theta}$. In the limit $h \to 0$ we expect all curves to tend to the constant 4. The plot thus provides evidence for second order convergence of all of the values throughout the evolution. All of the other primary BSSN variables as well as the dynamical scalar field quantities demonstrate the same convergence. (d) Direct verification that the metric found by numerically solving the BSSN equations satisfies Einstein's equations in their covariant form. Here the tr component of the residual $E^\mu{}_\nu$ defined in (72) is plotted for three different resolutions. Once more, higher resolution values have been rescaled so that overlap of the curves signals the expected $O(h^2)$ convergence of the residuals to 0. All of the plots correspond to evolution of strong subcritical initial data with $1 + \log$ slicing. For (a)–(b) the shift vector was set to 0, while in (c)–(d) it was evolved using the Gamma-driver condition (i.e. $\beta = \beta^G$).

typical of those used in our study, the Hamiltonian constraint is well preserved during such an evolution and, importantly, the deviations from conservation converge to zero at second order in the mesh spacing as expected.

The total mass content of the spacetime seen at spatial infinity (the ADM mass) is a conserved quantity. Here, using the G-BSSN variables the Misner-Sharp mass function is given by

$$M(r) = \frac{r\tilde{\gamma}_{\theta\theta}^{1/2}e^{2\phi}}{2}\left[1 - \frac{\tilde{\gamma}_{\theta\theta}}{\tilde{\gamma}_{rr}}\left(1 + r\frac{\partial_r\tilde{\gamma}_{\theta\theta}}{2\tilde{\gamma}_{\theta\theta}} + 2r\frac{\partial_r e^\phi}{e^\phi}\right)^2\right]. \quad (65)$$

The total mass, M_{ADM}, can be evaluated at the outer boundary,

$$M_{\text{ADM}} \equiv M(r = \infty). \quad (66)$$

The deviation of the total mass from its time average is plotted in Fig. 1(b); as the resolution of the numerical grid increases the variations converge to zero in a second order fashion.

2. Convergence test

As mentioned in Secs. III A and III C, we implemented our code using second order finite differencing of all spatial and temporal derivatives. Denoting any continuum solution component by $q(t, X)$, where X is the spatial coordinate, and a discrete approximation to it computed at finite difference resolution, h, by $q^h(t, X)$, to leading order in h we expect

$$q^h(t, X) = q(t, X) + h^2 e_2[q](t, X) + \cdots. \quad (67)$$

Fixing initial data, we perform a sequence of calculations with resolutions h, $h/2$ and $h/4$ and then compute a convergence factor, $C(t; q)$, defined by

$$C(t; q) = \frac{\|q^h(t, X) - q^{h/2}(t, X)\|_2}{\|q^{h/2}(t, X) - q^{h/4}(t, X)\|_2}, \quad (68)$$

where $\|\cdot\|_2$ is the l_2 norm, i.e. the RMS value. It is straightforward to argue from (67) that, for sufficiently small h, $C(t, q)$ should approach 4 if the solution *is* converging at second order. The values of the convergence factor for a selection of dynamical variables are plotted for a strong-data evolution in Fig. 1(c) and provide clear evidence that the solution is second order convergent throughout the time evolution.

3. Direct validation via Einstein's equations

A direct method to test the fidelity of our numerical solver involves the evaluation of a residual based on the *covariant* form of Einstein's equations. We start with a reconstruction of the four-dimensional metric in spherical symmetry,

$$ds^2 = (-\alpha^2 + \beta^2 a^2)dt^2 + 2a^2\beta dt dr + a^2 dr^2 + r^2 b^2 d\Omega^2, \quad (69)$$

using the primary G-BSSN variables, $\tilde{\gamma}_{ij}$ and ϕ. In particular, a and b are simply given by

$$a(t, r) = e^{4\phi(t,r)}\tilde{\gamma}_{rr}(t, r), \quad (70)$$

$$b(t, r) = e^{4\phi(t,r)}\tilde{\gamma}_{\theta\theta}(t, r). \quad (71)$$

We then check to see if the metric (69) satisfies the covariant Einstein equations (3) to the expected level of truncation error. Specifically, defining the residual

$$E^\mu_{\ \nu} \equiv G^\mu_{\ \nu} - 8\pi T^\mu_{\ \nu}, \quad (72)$$

and replacing all derivatives in G^μ_ν with second order finite differences, we expect $E^\mu_{\ \nu}$ to converge to zero as $O(h^2)$ as $h \to 0$.[4] Precisely this behavior is shown in Fig. 1(d). This is a particularly robust test of our implementation since the nontrivial components of the covariant Einstein equations are quite complicated and, superficially at least, algebraically independent of the BSSN equations. For instance, the *tr* component of the residual (72) is given by

$$E^t_{\ r} = \frac{2\beta}{r\alpha^2}\left(\frac{\partial_r a}{a} - 2\frac{\partial_r b}{b} + \frac{\partial_r\alpha}{\alpha}\right)$$
$$+ \frac{2\beta}{\alpha^2}\left(-\frac{\partial_r^2 b}{b} + \frac{\partial_r a\partial_r b}{ab} - \frac{(\partial_r\Psi)^2}{2} + \frac{\partial_r\alpha\partial_r b}{\alpha b}\right)$$
$$+ \frac{2}{\alpha^2}\left(\frac{\partial_t\partial_r b}{b} + \frac{\partial_r\Psi\partial_t\Psi}{2} - \frac{\partial_t a\partial_r b}{ab} - \frac{\partial_t b\partial_r\alpha}{\alpha b}\right)$$
$$+ \frac{2}{r\alpha^2}\left(-\frac{\partial_t a}{a} + \frac{\partial_t b}{b}\right) \quad (73)$$

and depends on all of the dynamical variables of the system. The observed convergence of the residual is only plausible if (1) our G-BSSN equations (14)–(18) have been correctly derived from the covariant Einstein equations, (2) we have discretized the geometric and matter equations properly, and (3) we have solved the full set of discretized equations correctly.

E. Finding black hole threshold solutions

The strength of the initial data can be set by adjusting the amplitude of the scalar field, p, in (42). For weak enough initial data (small enough p), the matter shell will reach the origin and then disperse, with the final state being a flat spacetime geometry. Strong enough initial data, on the other hand (large enough p), result in a matter

---

[4]Although it is not crucial for the usefulness of this test, we discretize the E^μ_ν using a difference scheme that is distinct from the one used in the main code.

concentration in the vicinity of the origin which is sufficiently self gravitating that a black hole forms. Using a binary search, we can find the threshold initial data, defined by $p = p^\star$, for which $p < p^\star$ results in dispersal while $p > p^\star$ yields black hole formation. At any stage of the calculation, the binary search is defined by two "bracketing" values, p_l and p_h, such that evolutions with $p = p_l$ and $p = p_h$ result in dispersal and black hole formation, respectively. It is convenient to define the amount of parameter tuning that has occurred by the dimensionless quantity

$$\delta p \equiv \frac{p_h - p_l}{p_l}. \qquad (74)$$

The dispersal case can be detected easily as the scalar field leaves the vicinity of the origin and the geometry approaches flat spacetime. To detect black hole formation, we use an apparent horizon finder to locate a surface $r =$ const on which the divergence of the outgoing null rays vanishes. We first define the divergence function

$$\Theta = q^{\mu\nu}\nabla_\mu k_\nu, \qquad (75)$$

where $q^{\mu\nu}$ is the induced metric on the constant r surface. In spherical symmetry with metric (69) we have

$$q_{\mu\nu} = \text{diag}(0, 0, r^2 b^2, r^2 b^2 \sin^2\theta), \qquad (76)$$

where k^μ is the null outgoing vector given by

$$k_\mu = \frac{1}{\sqrt{2}}[a\beta - \alpha, a, 0, 0]. \qquad (77)$$

Therefore, (75) becomes

$$\Theta = \frac{\sqrt{2}}{rb}\left(\frac{r}{\alpha}\partial_t(b) + \left(\frac{1}{a} - \frac{\beta}{\alpha}\right)\partial_r(rb)\right). \qquad (78)$$

The formation of an apparent horizon[5] is signaled by the value of the function Θ crossing zero at some radius and modulo cosmic censorship implies that the spacetime contains a black hole. We note that since the focus of our work was on the critical (threshold) solution we made no effort to continue evolutions beyond the detection of trapped surfaces.

IV. RESULTS

In this section we describe results from two sets of numerical experiments to study the efficacy of the G-BSSN formulation in the context of critical collapse. Again, our calculations use the standard $1 + \log$ slicing condition for

---

[5]Technically a marginally trapped surface—the apparent horizon being the outermost of these.

the lapse, and a shift which is either zero or determined from the Gamma-driver condition.

A. Zero shift

We first perform a collection of numerical experiments where the shift vector is set to zero. As described in Sec. III E, in principle we can find the black hole threshold solution $p \simeq p^\star$ using a binary search algorithm which at any stage is defined by two values p_l and p_h, with $p_l < p < p_h$, and where p_l corresponds to dispersal (weak data) while p_h corresponds to black hole formation (strong data).

As discussed in the introduction, the massless scalar collapse model has a very well-known critical solution, and we summarize the features most relevant to our study here. The threshold configuration is discretely self-similar with an echoing exponent measured from the first calculations to be $\Delta \approx 3.44$ [13]. Following the original studies, Gundlach [18] showed that the construction of the precisely discretely self-similar spacetime could be posed as an eigenvalue problem, the solution of which led to the more accurate value $\Delta = 3.4439 \pm 0.0004$. This estimate was subsequently improved by Martin-Garcia and Gundlach to $\Delta = 3.445452402(3)$ [23].

The original calculations determined a value $\gamma \approx 0.37$ for the mass-scaling exponent [13]; further work based on perturbation theory gave $\gamma \approx 0.374$ [19,22]. Here it is important to note that, as pointed out independently by Gundlach [19] and Hod and Piran [20], the simple power law scaling (1) gets modified for discretely self-similar critical solutions to

$$\ln M = \gamma \ln|p - p^\star| + c + f(\gamma \ln|p - p^\star| + c), \quad (79)$$

where f is a universal function with period Δ and c is a constant depending on the initial data. This results in the superposition of a periodic wiggle in the otherwise linear scaling of $\ln M$ as a function of $\ln|p - p^\star|$.

Finally, Garfinkle and Duncan [21] pointed out that near-critical scaling is seen in physical quantities other than the mass and, dependent on the quantity, in the subcritical as well as supercritical regime. In particular they argued that in subcritical evolutions the maximum central value, $\mathcal{R}_{\max}$, of the four-dimensional Ricci scalar, $\mathcal{R}$, defined by

$$\mathcal{R}_{\max} \equiv \max_t \mathcal{R}(0, t), \qquad (80)$$

should satisfy the scaling

$$\mathcal{R}_{\max} \sim |p - p^\star|^{-2\gamma}, \qquad (81)$$

where the factor -2 in the scaling exponent can be deduced from the fact that the curvature has units of length^{-2}. For the discretely self-similar case this scaling law is also modulated by a wiggle with period $\Delta/(2\gamma)$, which for the massless scalar field is about 4.61.

Using initial data given by (42) we tune p so that it is close to the critical value: typically this involves reducing the value of δp defined by (74) so that it is about 10^{-12}, which is a few orders of magnitude larger than machine precision. Our implementation includes code that actively monitors the dynamical variables for any indications of coordinate singularities or other pathologies which could cause the numerical solver to fail. Provided that such pathologies do not develop, we expect to observe features characteristic of critical collapse—discrete self-similarity and mass scaling in particular—to emerge as $p \to p^\star$.

One way the discrete self-similarity of the critical solution is manifested is as a sequence of echoes—oscillations of the scalar field near the origin such that after each oscillation the profile of the scalar field is repeated but on a scale $\exp(\Delta)$ smaller than that of the preceding echo [see Eq. (2)]. The oscillations are similarly periodic in the logarithmic time scale $\ln(T^\star - T)$, where T is the proper time measured at the origin,

$$T(t) \equiv \int_0^t \alpha(\hat{t}, 0) d\hat{t}, \tag{82}$$

and $T^\star$ is the accumulation time at which the singularity forms (always at $r = 0$). Furthermore, viewed at the origin, the oscillations of the scalar field occur at a fixed amplitude of about 0.61 (with our units and conventions for the Einstein's equations). As shown in Fig. 2, when we tune the initial data to the critical value, the central value of scalar field exhibits oscillatory behavior and the amplitude is close to the expected value. The anticipated periodicity in logarithmic time is also apparent with a measured $\Delta = 3.43 \pm 0.02$, in agreement with previous results. We thus have strong evidence that the evolution has indeed approached the critical regime and that the measured oscillations are true echoes rather than numerical artifacts.

Evidence that our code correctly captures the expected critical scaling behavior (81) of $\mathcal{R}_{\max}$ is presented in Fig. 3. We find $\gamma = 0.38 \pm 0.01$, consistent with previous calculations. We note that we can measure scaling from our computations up to $\ln|p - p^\star| = -29$ (or $|p - p^\star| \approx 10^{-13}$). However, in Fig. 3 we have excluded the last few values closest to the critical point from both the plot and the linear fit: specifically, we truncate the fit at $\ln|p - p^\star| = -25$. The rationale for this is that we use the largest subcritical value of p as an approximation to the critical value $p^\star$ rather than, for example, implementing a multiparameter fit that includes $p^\star$ as one of the parameters. Our estimate of $p^\star$ thus has an intrinsic error of $e^{-29} \approx 10^{-13}$ and by fitting to data with $\ln|p - p^\star| \geq -25$ we render the error in the $p^\star$ estimate essentially irrelevant. We note that consistent with the early observations of the robustness of mass scaling in the model [13], measuring the exponent γ can be achieved by moderate tuning, in this case $\ln|p - p^\star| \approx -9$, (i.e. $\delta p \approx 10^{-3}$). However, to be able to observe the echoing
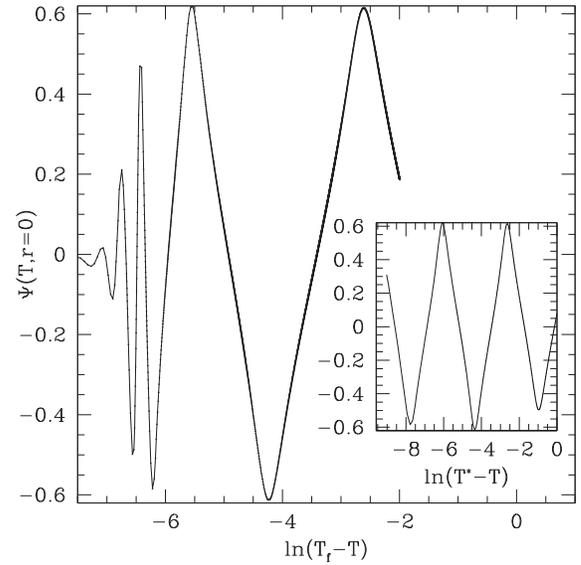

FIG. 2.   Echoing behavior in the scalar field for a marginally subcritical evolution with $\delta p \approx 10^{-12}$. The main plot displays the central value of the scalar field versus a logarithmically scaled time parameter, $\ln(T_f - T)$, where T is central proper time and T_f is the approximate value of that time when near-critical evolution ceases and the total dispersal of the pulse to infinity begins. This particular scaling is chosen solely to more clearly demonstrate the evolution of the central value of Ψ during the critical phase through to dispersal. Note that our choice of abscissa means that evolution proceeds from right to left. The inset also plots Ψ at $r = 0$ but now in the "natural" logarithmic time coordinate $\tau \equiv \ln(T^\star - T)$ where $T^\star$ is the "accumulation time" at which the solution becomes singular and which has been estimated based on the positions of the extrema in Ψ. The amplitude of the scalar field at the origin oscillates between $(-0.61, 0.61)$, consistent with the calculations reported in [13]. The data yield an echoing exponent of $\Delta = 3.43 \pm 0.02$ which is in agreement with the value $\Delta = 3.445452402(3)$ Martin-Garcia and Gundlach have computed by treating the computation of the precisely critical solution as an eigenvalue problem [23].

exponent (the oscillations around the fitting line, for example) we need to tune much closer to the critical value.

The echoing behavior of the critical solution is also reflected in the geometry of spacetime and the matter variables other than the scalar field. Figure 4 shows the radial profile of the G-BSSN variable ϕ at an instant close to the accumulation time $T^\star$. As seen in this plot, fine structure develops in the function in the near-critical regime. Observe that from the definition (7) and the choice (28), the scalar ϕ is the ratio of the determinant of the 3-metric, γ, to the determinant of the flat metric, $\mathring{\gamma}$:

$$\phi = \frac{1}{12} \ln(\gamma / \mathring{\gamma}). \tag{83}$$

The radial matter density, $dm/dr = r^2 \rho$, is a convenient diagnostic quantity for viewing near-critical evolution.
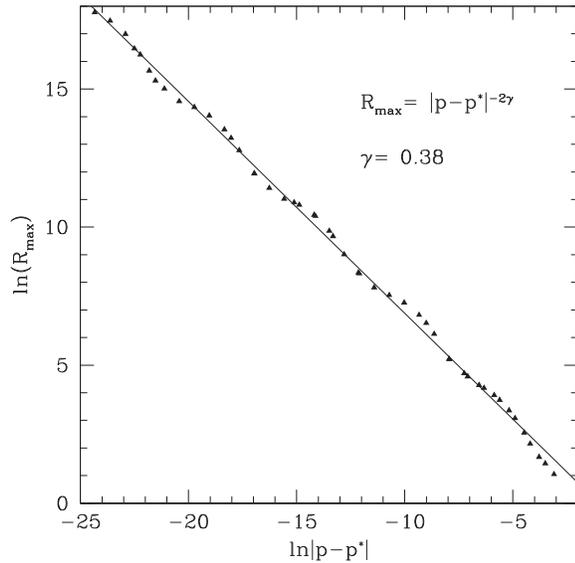
FIG. 3.   The maximum central value, $\mathcal{R}_{max}$, of the four-dimensional Ricci scalar, $\mathcal{R}$, attained during subcritical evolution as a function of the logarithmic distance $\ln|p - p^{\star}|$ of the tuning parameter from the critical value. As first observed in [21] the Ricci scalar scales as $R \sim |p - p^{\star}|^{-2\gamma}$, where γ is the universal mass-scaling exponent in (1). The value $\gamma = 0.38 \pm 0.01$ computed via a least squares fit is in agreement with the original calculations [13] as well as many other subsequent computations. We note that the oscillations of the data about the linear fit are almost certainly genuine, at least in part. As discussed in the text, we *expect* a periodic wiggle in the data with period $\Delta/(2\gamma) \approx 4.61$. Performing a Fourier analysis of the residuals to the linear fit we find a peak at about 4 with a bandwidth of approximately 1, consistent with that expectation. As described in more detail in the text, although we have data from computations with $\ln|p - p^{\star}| < -25$, we do not include it in the fit. The naive method we use to estimate $p^{\star}$ means that the relative uncertainty in $p - p^{\star}$ grows substantially as $p \rightarrow p^{\star}$ so that inclusion of the data from the most nearly critical calculations will corrupt the overall fit.

Snapshots of this function from a typical marginally subcritical calculation are shown in Fig. 5: the echoing behavior is clearly evident in the sequence. The number of echoes is dependent on the degree to which the solution has been tuned to criticality. In this case, where $\delta p = 10^{-12}$, we expect and see about four echoes (last frame of the figure). Here we note that each of the echoes in dm/dr corresponds to half of one of the scalar field oscillations shown in Fig. 2 (where the inset shows about $2\frac{1}{2}$ full cycles).

Figure 6(a) plots the central matter density $\rho(t, 0)$ for a marginally supercritical calculation. In accord with the self-similar nature of the near-critical solution, the central density grows exponentially with time. Figure 6(b) is a snapshot of the extrinsic curvature at the critical time $t \approx t^{\star}$ while Fig. 6(c) shows the dynamics of the central value of the lapse function and compares it with α from the calculations performed with $\beta = \beta_G$ described in the next
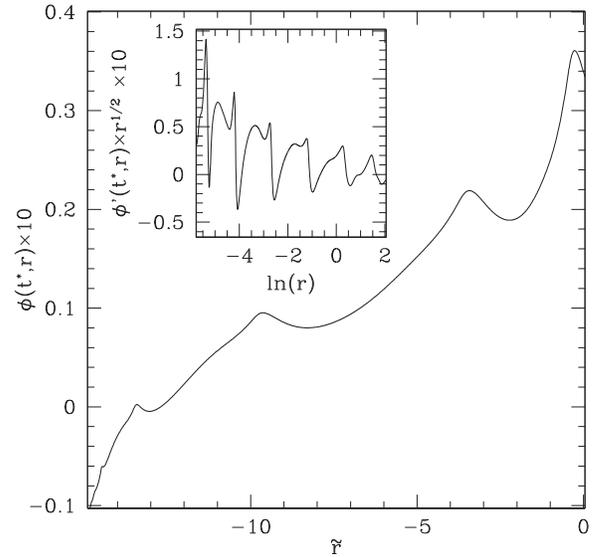

FIG. 4.   Discrete self-similarity of the geometry of spacetime in the black hole threshold evolution previously discussed in Fig. 2. Here, the G-BSSN variable ϕ is plotted as a function of the computational radial coordinate $\tilde{r}$ at the accumulation time $t^{\star}$. Note that from (83) ϕ measures the deviation of the determinant of the 3-metric from that of a flat metric. The inset graph is the radial derivative of ϕ scaled by $\sqrt{r}$ to highlight the formation of fine structure in the geometry of the critical solution. The approximate periodicity of $\sqrt{r}\phi'$ in $\ln(r)$ (modulo an overall varying scale) provides weak evidence that the coordinate system used in the calculation adapts to the self-similarity of the critical solution.

section. Figure 6(d) displays the profile of the lapse at the critical time.

We note that we have not fully resolved the critical behavior in the sense of having tuned p to the limit of machine precision, $\delta p \approx 10^{-16}$, which would capture roughly two additional echoes in the threshold solution (one full echo in the scalar field). In principle, by setting N_r sufficiently large we could almost certainly do so since there are no indications that our method would break down at higher resolution and closer to criticality. However, we estimate that the required computing time for a complete critical search would increase from weeks to several months and we have thus not done this. Ultimately, a more effective approach to enhancing the resolution would be to incorporate a technique such as adaptive mesh refinement into our solver.

The results displayed in Figs. 2–6 provide strong evidence that the coordinate system consisting of $1 + \log$ lapse and zero shift remains nonsingular in the critical regime, at least for the range of scales probed for $\delta p \approx 10^{-12}$. Additionally, the approximate periodicity in $\ln(r)$ that can be seen, for example, in $\sqrt{r}\phi'$ (Fig. 4) and dm/dr (Fig. 5) suggests that the coordinates may be adapting to the self-similarity. Whether or not this is actually the case is a matter requiring further study.
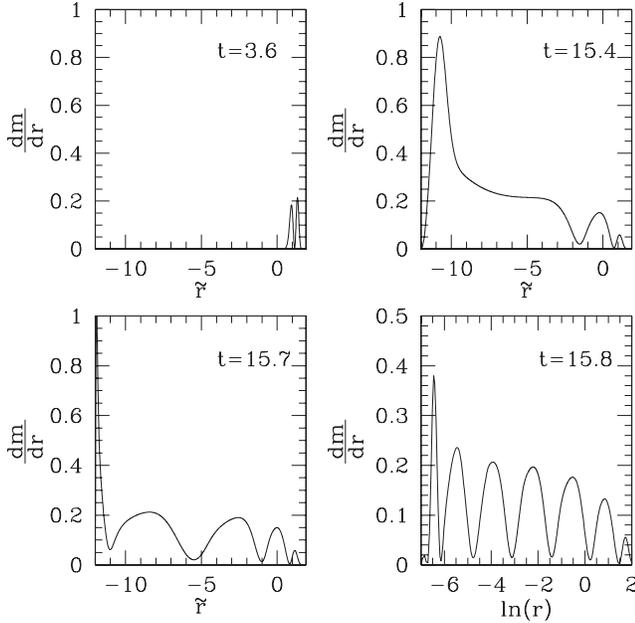
FIG. 5.   Snapshots of radial mass density for a marginally subcritical calculation ($\delta p \approx 10^{-12}$, $N_r = 2048$). Plotted is $dm/dr = r^2 \rho(t, r)$ where ρ is defined by (24). In this calculation $\beta = 0$ so we also have $dm/dr = T^t{}_t$. As the solution evolves, development of echoes is clearly seen. In the final frame, which is at an instant $t = 15.8$ that is close to the accumulation time $t^\star$, we observe four echoes. Note that we count neither the tall thin peak at the extreme left nor the first two peaks on the right as echoes. The skinny peak will develop into an echo as p is tuned closer to $p^\star$. The two peaks on the right account for the bulk of the matter and represent the part of the initial pulse that implodes through the origin and then disperses "promptly," i.e. without participating in the strongly self-gravitating dynamics. A corresponding plot for an evolution far from criticality would contain *only* those two peaks. Note that the first three plots use the computational coordinate $\tilde{r}$ to provide a sense of the actual numerical calculation, while the last plot uses $\ln(r)$ in order to best highlight the discrete self-similarity of the threshold solution. As is the case for the data plotted in the inset of the previous figure, the approximate periodicity of the mass density in $\ln(r)$ suggests that the coordinates are adapting to the self-symmetry of the critical spacetime.

B. Gamma-driver shift

We now briefly report on experiments similar to those of the previous section but where the shift was evolved with the Gamma-driver condition (38). A principal observation is that this gauge also facilitates near-critical evolutions with results similar to the $\beta = 0$ choice. In particular, we are again able to observe all of the characteristics of the black hole threshold solution.

The gauge condition (38) acts as a damping factor for the conformal connection, $\tilde{\Lambda}^i$, and we would therefore expect to observe a significant change in the profile of $\tilde{\Lambda}^i$ at threshold relative to the zero-shift case. This expectation is borne out by the comparison illustrated in Figs. 7(a)–7(b).
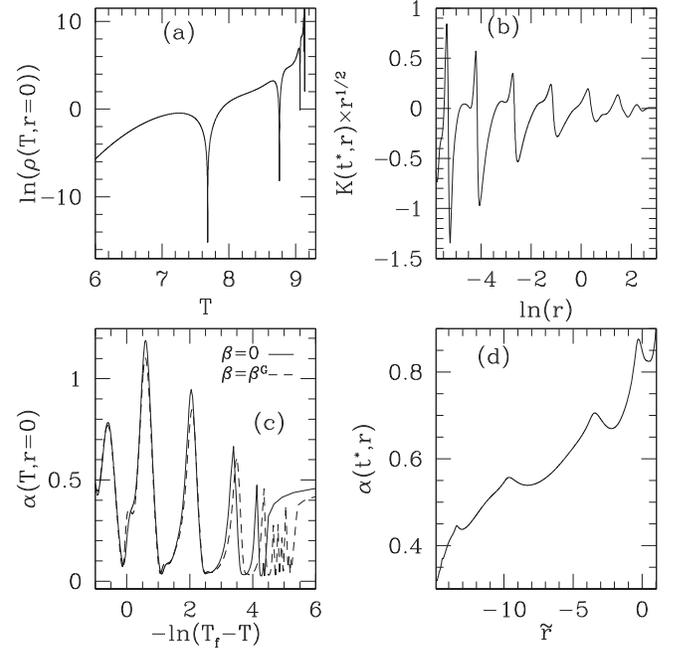
FIG. 6.   Profiles of matter and geometry variables from strongly gravitating, near-critical evolutions where the echoing behavior emerges. Results were computed using $1 + \log$ slicing and zero shift, except for the dashed curve in (c) where $\beta = \beta^G$. (a) Central energy density, $\rho(T, 0)$, as a function of proper central time, T, and in logarithmic scale for a supercritical evolution. The density oscillates and grows exponentially as the system approaches the critical solution and then eventually collapses to form a black hole. (b) Profile of the extrinsic curvature, $K(t^\star, r)$, scaled by $r^{1/2}$ in order to make the echoing behavior more visible, where $t^\star$ denotes a time very close to the accumulation time. The evolution is marginally subcritical in this case. (c) Central value of the lapse function, α, during subcritical evolutions with $\beta = 0$ (solid) and $\beta = \beta_G$ (dashed). The plots use a logarithmically transformed proper time variable, $-\ln(T_f - T)$, where T_f is the approximate time at which the final dispersal of the pulse from the origin begins. In both cases α exhibits echoing and there is no evidence of pathological behavior, such as the lapse collapsing or becoming negative. The close agreement of α for the two choices of β indicates that the time slicing varies little between the two coordinate systems. Note that there are three extra oscillations for the $\beta = \beta_G$ case, in the time interval $-\ln(T_f - T) \gtrsim 4.5$. These are spurious and due to a lack of finite difference resolution; there are only six time steps in each oscillation. (d) Radial profile $\alpha(t^\star, r)$ at a time $t = t^\star$ which is close to the accumulation time and when the self-similarity and echoing in the spacetime geometry is apparent.

When $\beta = 0$, $\tilde{\Lambda}^i$ diverges as $1/r$ close to the origin while it appears to have finite amplitude for $\beta = \beta^G$. We find that the shift develops very sharp oscillations near the origin; some typical behavior can be seen in the plot of $\beta'(t, 0)$ shown in Fig. 7(c). We believe that these oscillations are genuine and our expectation is that $\beta'(t, 0)$ will diverge in the precise critical limit. Further, we observe that the oscillations can create numerical artifacts and generally
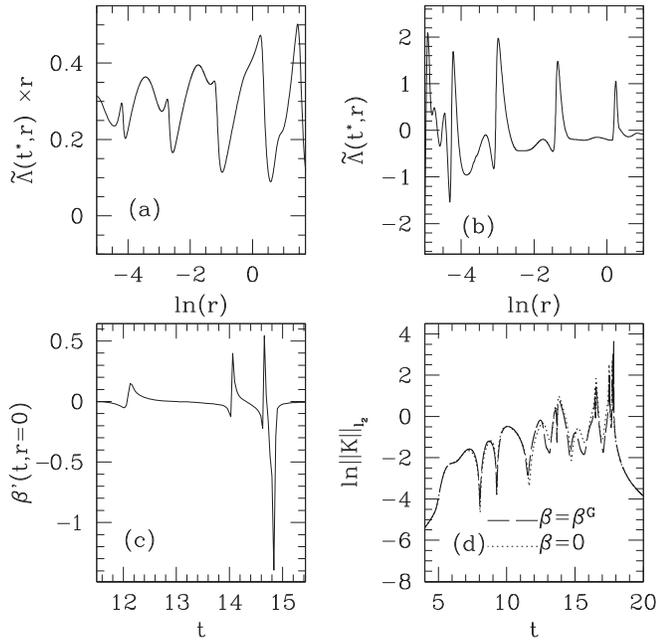
FIG. 7. Profiles of various G-BSSN variables from marginally subcritical evolutions. (a) Profile of the conformal connection $\hat{\Lambda}$ as computed with $\beta = 0$ and at a time $t^\star$ close to the accumulation time. Note that the function has been scaled by r and in fact diverges like $1/r$. (b) Profile of $\tilde{\Lambda}$ as computed with $\beta = \beta^G$, again at a moment close to the accumulation time. Here the $1/r$ growth seen when the condition $\beta = 0$ is adopted is absent. (c) Profile of the central spatial derivative of the shift vector, $\beta'(t, 0)$, as computed with $\beta = \beta^G$. As the echoes develop closer to the origin, β' increases and presumably will diverge in the continuum, precisely critical limit. (d) Time development of the l_2-norm of the extrinsic curvature during subcritical evolutions for both the $\beta = 0$ and $\beta = \beta^G$ calculations. In both cases the extrinsic curvature develops a divergent profile near $r = 0$ in the critical regime.

require higher resolution relative to the $\beta = 0$ case, as well as dissipation, to be controlled. Indeed, when using the Gamma-driver condition we find that Kreiss/Oliger dissipation is crucial to suppress unresolved high frequency oscillations close to the origin. Figure 7(d) shows the growth in the norm of the extrinsic curvature during a subcritical evolution. The norm of K does not exhibit any significant difference for the two choices of the shift.

As was the case for the $\beta = 0$ calculations, the results shown in Figs. 6–7 strongly suggest that the combination of $1 + \log$ slicing and Gamma-driver shift provides a coordinate system which is adequate for computing the near-critical solution. In addition, the approximate periodicity seen in Figs. 6(b)–6(c) and 7(a)–7(b) suggests that this gauge may also be adapting to the self-symmetry.

V. CONCLUSION

We have described a numerical code that implements a generalized BSSN formulation adapted to spherical symmetry. Using standard dynamical coordinate choices,

including $1 + \log$ slicing and a shift which either vanished or satisfied a Gamma-driver condition, we focused specifically on the applicability of the formulation and the gauge choices to studies of type II critical phenomena. As a test of the approach we revisited the model of massless scalar collapse, where the properties of the critical solution are very well known from previous work. For both choices of the shift, we found that our code was able to generate evolutions that were very close to criticality so that, in particular, we could observe the expected discrete self-similarity of the critical solution. To our knowledge, this is the first fully evolutionary implementation of a hyperbolic formulation of Einstein's equations that has been able to unequivocally resolve discrete self-similarity in type II collapse. Furthermore, measured properties from near-critical solutions, including the mass-scaling and echoing exponents, are in agreement with previous work. Our results strongly suggest that the G-BSSN formulation, in conjunction with standard dynamical coordinate conditions, is capable of evolving the spacetime near criticality without the development of coordinate pathologies. There is also some evidence that both gauges adapt to the self-similarity, but we have not yet studied this issue in any detail.

We found that certain primary G-BSSN variables diverge as the critical solution is approached: this is only to be expected since the precisely critical solution contains a naked singularity. Dealing with such solution features in a stable and accurate manner presents a challenge for any code and in our case we found that a combination of a nonuniform grid and Kreiss/Oliger dissipation was crucial. Our use of a time-implicit evolution scheme may have also been important although we did not experiment with that aspect of our implementation. However, we suspect that the implicit time-stepping helped maintain regularity of the solutions near $r = 0$, as other researchers have found.

Given the success of the G-BSSN approach, it is natural to consider its generalization and application to settings with less symmetry, but where curvilinear coordinates are still adopted. In particular, one axisymmetric problem that has yet to be resolved is the collapse of pure gravity waves. This scenario arguably provides the most fundamental critical phenomena in gravity as the behavior must be intrinsic to the Einstein equations, rather than being dependent on some matter source. Critical collapse of gravitational waves—-with mass scaling and echoing— was observed by Abrahams and Evans over 20 years ago [27]. However, their original results have proven very difficult to reproduce (or refute) [28–31,34]. We refer the reader to the recent paper by Hilditch *et al.* [34] for detailed discussions concerning some apparent inconsistencies among the follow-up studies, as well as the challenges and complications involved in evolving various types of nonlinear gravitational waves. We are currently extending the methodology described above to the axisymmetric case with plans to use the resulting code to study vacuum collapse. Results from this undertaking will be reported in a future paper.

APPENDIX A: BSSN IN SPHERICAL SYMMETRY

In this appendix, we provide the explicit expressions of the G-BSSN evolution equations in spherical symmetry.

The evolution equations (14)–(15) for ϕ and the components of the conformal metric $\tilde{\gamma}_{ij}$ simplify to

$$\partial_t\phi = \frac{1}{6}\alpha K + \beta\partial_r\phi + \sigma\frac{1}{6}\mathcal{B}, \tag{A1}$$

$$\partial_t\tilde{\gamma}_{rr} = -2\alpha\tilde{A}_{rr} + \beta\partial_r\tilde{\gamma}_{rr} + 2\tilde{\gamma}_{rr}\partial_r\beta - \sigma\frac{2}{3}\tilde{\gamma}_{rr}\mathcal{B}, \tag{A2}$$

$$\partial_t\tilde{\gamma}_{\theta\theta} = -2\alpha\tilde{A}_{\theta\theta} + \beta\partial_r\tilde{\gamma}_{\theta\theta} + 2\frac{\beta}{r}\tilde{\gamma}_{\theta\theta} - \sigma\frac{2}{3}\tilde{\gamma}_{\theta\theta}\mathcal{B}, \tag{A3}$$

where $\mathcal{B}$ is the divergence of the shift vector,

$$\mathcal{B}(t,r) = D_i\beta^i = \partial_r\beta + \frac{2\beta}{r} + \beta\left(\frac{\partial_r\tilde{\gamma}_{rr}}{2\tilde{\gamma}_{rr}} + \frac{\partial_r\tilde{\gamma}_{\theta\theta}}{\tilde{\gamma}_{\theta\theta}}\right). \tag{A4}$$

To display the equation of motion for the trace of the extrinsic curvature K and $\tilde{A}_{ij}$ we first define

$$\mathcal{D}_{ij} \equiv D_iD_j\alpha, \tag{A5}$$

which has two independent components,

$$\mathcal{D}_{rr} = \partial_r^2\alpha - \partial_r\alpha\left(\frac{\partial_r\tilde{\gamma}_{rr}}{\tilde{\gamma}_{rr}} + 4\partial_r\phi\right), \tag{A6}$$

$$\mathcal{D}_{\theta\theta} = r\partial_r\alpha\frac{\tilde{\gamma}_{\theta\theta}}{\tilde{\gamma}_{rr}} + \frac{r^2}{2}\partial_r\alpha\left(\frac{\partial_r\tilde{\gamma}_{\theta\theta}}{\tilde{\gamma}_{rr}} + 4\partial_r\phi\frac{\tilde{\gamma}_{\theta\theta}}{\tilde{\gamma}_{rr}}\right). \tag{A7}$$

The trace of $\mathcal{D}_{ij}$ is

$$\mathcal{D} \equiv \gamma^{ij}\mathcal{D}_{ij} = e^{-4\phi}\left(\frac{\mathcal{D}_{rr}}{\tilde{\gamma}_{rr}} + 2\frac{\mathcal{D}_{\theta\theta}}{r^2\tilde{\gamma}_{\theta\theta}}\right). \tag{A8}$$

Then the evolution of K is given by

$$\partial_t K = -\mathcal{D} + \alpha\left(\frac{1}{3}K^2 + \frac{\tilde{A}_{rr}^2}{\tilde{\gamma}_{rr}^2} + 2\frac{\tilde{A}_{\theta\theta}^2}{\tilde{\gamma}_{\theta\theta}^2}\right)$$
$$+ \beta\partial_r K + 4\pi\alpha(\rho + S) \tag{A9}$$

and the evolution equations for the traceless part of the extrinsic curvature are

$$\partial_t\tilde{A}_{rr} = e^{-4\phi}[-\mathcal{D}_{rr}^{\mathrm{TF}} + \alpha(R_{rr}^{\mathrm{TF}} + 8\pi S_{rr}^{\mathrm{TF}})]$$
$$+ \alpha\left(\tilde{A}_{rr}K - \frac{2\tilde{A}_{rr}^2}{\tilde{\gamma}_{rr}}\right)$$
$$+ 2\tilde{A}_{rr}\partial_r\beta + \beta\partial_r\tilde{A}_{rr} - \sigma\frac{2}{3}\mathcal{B}\tilde{A}_{rr}, \tag{A10}$$

$$\partial_t\tilde{A}_{\theta\theta} = \frac{e^{-4\phi}}{r^2}[-\mathcal{D}_{\theta\theta}^{\mathrm{TF}} + \alpha(R_{\theta\theta}^{\mathrm{TF}} + 8\pi S_{\theta\theta}^{\mathrm{TF}})]$$
$$+ \alpha\left(\tilde{A}_{\theta\theta}K - 2\frac{\tilde{A}_{\theta\theta}^2}{\tilde{\gamma}_{\theta\theta}}\right)$$
$$+ 2\frac{\beta}{r}\tilde{A}_{\theta\theta} + \beta\partial_r\tilde{A}_{\theta\theta} - \sigma\frac{2}{3}\tilde{A}_{\theta\theta}\mathcal{B}, \tag{A11}$$

where R denotes the 3-Ricci tensor with nonvanishing components

$$R_{rr} = \frac{3(\partial_r\tilde{\gamma}_{rr})^2}{4\tilde{\gamma}_{rr}^2} - \frac{(\partial_r\tilde{\gamma}_{\theta\theta})^2}{2\tilde{\gamma}_{\theta\theta}^2} + \tilde{\gamma}_{rr}\partial_r\tilde{\Lambda} + \frac{1}{2}\partial_r\tilde{\gamma}_{rr}\tilde{\Lambda}$$
$$+ \frac{1}{r}\left(4\partial_r\phi - \frac{\partial_r\tilde{\gamma}_{rr} - 2\partial_r\tilde{\gamma}_{\theta\theta}}{\tilde{\gamma}_{\theta\theta}} - \frac{2\tilde{\gamma}_{rr}\partial_r\tilde{\gamma}_{\theta\theta}}{\tilde{\gamma}_{\theta\theta}^2}\right)$$
$$- 4\partial_r^2\phi + 2\partial_r\phi\left(\frac{\partial_r\tilde{\gamma}_{rr}}{\tilde{\gamma}_{rr}} - \frac{\partial_r\tilde{\gamma}_{\theta\theta}}{\tilde{\gamma}_{\theta\theta}}\right)$$
$$- \frac{\partial_r^2\tilde{\gamma}_{rr}}{2\tilde{\gamma}_{rr}} + \frac{2(\tilde{\gamma}_{rr} - \tilde{\gamma}_{\theta\theta})}{r^2\tilde{\gamma}_{\theta\theta}}, \tag{A12}$$

$$R_{\theta\theta} = \frac{r^2\tilde{\gamma}_{\theta\theta}}{\tilde{\gamma}_{rr}}\left(\partial_r\phi\frac{\partial_r\tilde{\gamma}_{rr}}{\tilde{\gamma}_{rr}} - 2\partial_r^2\phi - 4(\partial_r\phi)^2\right)$$
$$+ \frac{r^2}{\tilde{\gamma}_{rr}}\left(\frac{(\partial_r\tilde{\gamma}_{\theta\theta})^2}{2\tilde{\gamma}_{\theta\theta}} - 3\partial_r\phi\partial_r\tilde{\gamma}_{\theta\theta} - \frac{1}{2}\partial_r^2\tilde{\gamma}_{\theta\theta}\right)$$
$$+ r\left(\tilde{\Lambda}\tilde{\gamma}_{\theta\theta} - \frac{\partial_r\tilde{\gamma}_{\theta\theta}}{\tilde{\gamma}_{\theta\theta}} - \frac{6\partial_r\phi\tilde{\gamma}_{\theta\theta}}{\tilde{\gamma}_{rr}}\right)$$
$$+ \frac{\tilde{\gamma}_{\theta\theta}}{\tilde{\gamma}_{rr}} - 1. \tag{A13}$$

In the above expressions the superscript TF denotes application of the trace-free-part operator, whose action can be written explicitly as

$$X_{rr}^{\mathrm{TF}} = X_{rr} - \frac{1}{3}\gamma_{rr}X = \frac{2}{3}\left(X_{rr} - \frac{\gamma_{rr}X_{\theta\theta}}{\gamma_{\theta\theta}r^2}\right), \tag{A14}$$

$$X_{\theta\theta}^{\mathrm{TF}} = X_{\theta\theta} - \frac{1}{3}\gamma_{\theta\theta}X = \frac{1}{3}\left(X_{\theta\theta} - \frac{\gamma_{\theta\theta}X_{rr}}{\gamma_{rr}}\right). \tag{A15}$$

Here X represents any of the tensors $\mathcal{D}$, R or S.

Finally, the evolution of $\tilde{\Lambda}^i$ reduces to

$$
\begin{aligned}
\partial_t \tilde{\Lambda} = & \beta \partial_r \tilde{\Lambda} - \partial_r \beta \tilde{\Lambda} + \frac{2\alpha}{\tilde{\gamma}_{rr}} \left(\frac{6 \tilde{A}_{\theta\theta} \partial_r \phi}{\tilde{\gamma}_{rr}} - 8\pi S_r - \frac{2}{3} \partial_r K \right) \\
& + \frac{\alpha}{\tilde{\gamma}_{rr}} \left(\frac{\partial_r \tilde{\gamma}_{rr} \tilde{A}_{rr}}{\tilde{\gamma}_{rr}^2} - \frac{2\partial_r \tilde{\gamma}_{\theta\theta} \tilde{A}_{\theta\theta}}{\tilde{\gamma}_{\theta\theta}^2} + 4 \tilde{A}_{\theta\theta} \frac{\tilde{\gamma}_{rr} - \tilde{\gamma}_{\theta\theta}}{r \tilde{\gamma}_{\theta\theta}^2} \right) \\
& + \sigma \left(\frac{2}{3} \tilde{\Lambda} \mathcal{B} + \frac{\partial_r \mathcal{B}}{3 \tilde{\gamma}_{rr}} \right) + \frac{2}{r \tilde{\gamma}_{\theta\theta}} \left(\partial_r \beta - \frac{\beta}{r} \right) \\
& - 2 \frac{\partial_r \alpha \tilde{A}_{rr}}{\tilde{\gamma}_{rr}^2}.
\end{aligned} \tag{A16}
$$

APPENDIX B: SCALAR FIELD DYNAMICS AND ENERGY-MOMENTUM TENSOR IN SPHERICAL SYMMETRY

Here we present the evolution equations of a complex scalar field, with an arbitrary potential V, minimally coupled to gravity. The governing equations for a massless real scalar field follow as a special case where the imaginary part of the field and the potential are both set to zero.

The geometry of spacetime is given by a generic metric in spherical symmetry:

$$
ds^2 = (-\alpha^2 + \beta^2 a^2) dt^2 + 2a^2 \beta dt dr + a^2 dr^2 + r^2 b^2 d\Omega^2, \tag{B1}
$$

where a, b, α and β are all functions of t and r and where a and b are related to the primary BSSN variables via $a = \tilde{\gamma}_{rr} \exp(4\phi)$ and $b = \tilde{\gamma}_{\theta\theta} \exp(4\phi)$.

The complex scalar field is given in terms of real and imaginary parts, Ψ_R and Ψ_I, respectively,

$$
\Psi = \Psi_R(t, r) + i\Psi_I(t, r), \tag{B2}
$$

and has an associated energy-momentum tensor

$$
\begin{aligned}
T_{\mu\nu} = & \nabla_\mu \nabla_\nu \Psi_R - \frac{1}{2} g_{\mu\nu} \nabla^\eta \Psi_R \nabla_\eta \Psi_R \\
& + \nabla_\mu \nabla_\nu \Psi_I - \frac{1}{2} g_{\mu\nu} \nabla^\eta \Psi_I \nabla_\eta \Psi_I \\
& - \frac{1}{2} g_{\mu\nu} V(|\Psi|).
\end{aligned} \tag{B3}
$$

The evolution of the real part of the scalar field can be reduced to a pair of first-order-in-time equations via the definition

$$
\Xi_R \equiv \frac{b^2 a}{\alpha} (\partial_t \Psi_R - \beta \partial_r \Psi_R). \tag{B4}
$$

We then find the following evolution equations for Ψ_R and Ξ_R:

$$
\partial_t \Psi_R = \frac{\alpha}{b^2 a} \Xi_R + \beta \partial_r \Psi_R, \tag{B5}
$$

$$
\begin{aligned}
\partial_t \Xi_R = & \frac{\alpha b^2}{a} \left(\partial_r^2 \Psi_R + 2 \frac{\partial_r \Psi_R}{r} \right) + \partial_r \Psi_R \partial_r \left(\frac{\alpha b^2}{a} \right) \\
& + \beta \partial_r \Xi_R + \Xi_R \partial_r \beta + \Xi_R \frac{2\beta}{r} - a\alpha b^2 \partial_{|\Psi|}^2 V(|\Psi|).
\end{aligned} \tag{B6}
$$

The evolution equations for Ψ_I and Ξ_I follow from the index substitutions $R \leftrightarrow I$ in the right-hand sides of (B5)–(B6), respectively.

The matter source terms in the G-BSSN equations, namely ρ, S, S^i, S_{ij}, can be simplified by defining Π and Φ as

$$
\Pi \equiv \frac{a}{\alpha} (\partial_t \Psi - \beta \partial_r \Psi) \equiv \Pi_R(t, r) + i\Pi_I(t, r), \tag{B7}
$$

$$
\Pi_R = \frac{a}{\alpha} (\partial_t \Psi_R - \beta \partial_r \Psi_R) = \frac{\Xi_R}{b^2}, \tag{B8}
$$

$$
\Pi_I = \frac{a}{\alpha} (\partial_t \Psi_I - \beta \partial_r \Psi_I) = \frac{\Xi_I}{b^2}, \tag{B9}
$$

$$
\Phi \equiv \partial_r \Psi \equiv \Phi_R(t, r) + i\Phi_I(t, r), \tag{B10}
$$

$$
\Phi_R = \partial_r \Psi_R, \tag{B11}
$$

$$
\Phi_I = \partial_r \Psi_I. \tag{B12}
$$

Using these definitions, the variables ρ and S are given by

$$
\rho(t, r) = \frac{|\Pi|^2 + |\Phi|^2}{2a^2} + \frac{V(|\Psi|)}{2}, \tag{B13}
$$

$$
S(t, r) = \frac{3|\Pi|^2 - |\Phi|^2}{2a^2} - \frac{3}{2} V(|\Psi|). \tag{B14}
$$

In spherical symmetry, S^i has only a radial component,

$$
S^i = [S^r(t, r), 0, 0], \tag{B15}
$$

with

$$
S^r = - \frac{\Pi_R \Phi_R + \Pi_I \Phi_I}{a}. \tag{B16}
$$

Similarly, the spatial stress tensor, S_{ij}, has only two independent components,

$$
S_{ij} = \begin{pmatrix} S_{rr}(t, r) & 0 & 0 \\ 0 & r^2 S_{\theta\theta} & 0 \\ 0 & 0 & r^2 \sin^2 \theta S_{\theta\theta} \end{pmatrix}, \tag{B17}
$$

with

$$
S_{rr} = \frac{|\Pi|^2 + |\Phi|^2}{2} - a^2 \frac{V(|\Psi|)}{2}, \tag{B18}
$$

$$
S_{\theta\theta} = b^2 \left(\frac{|\Pi|^2 - |\Phi|^2}{2a^2} - \frac{V(|\Psi|)}{2} \right). \tag{B19}
$$

[1] M. Shibata and T. Nakamura, Phys. Rev. D **52**, 5428 (1995).

[2] T. W. Baumgarte and S. L. Shapiro, Phys. Rev. D **59**, 024007 (1998).

[3] R. Arnowitt, S. Deser, and C. W. Misner, in *Gravitation: An Introduction to Current Research*, edited by L. Witten (Wiley, New York, 1962).

[4] O. Sarbach, G. Calabrese, J. Pullin, and M. Tiglio, Phys. Rev. D **66**, 064002 (2002).

[5] G. Yoneda and H. Shinkai, Phys. Rev. D **66**, 124003 (2002).

[6] M. Campanelli, C. Lousto, P. Marronetti, and Y. Zlochower, Phys. Rev. Lett. **96**, 111101 (2006).

[7] J. G. Baker, J. Centrella, D.-I. Choi, M. Koppitz, and J. van Meter, Phys. Rev. Lett. **96**, 111102 (2006).

[8] M. Choptuik, L. Lehner, and F. Pretorius, in *General Relativity and Gravitation: A Centennial Perspective*, edited by A. Ashtekar, B. Berger, J. Isenberg, and M. MacCallum (Cambridge University Press, Cambridge, 2015).

[9] C. Bona, J. Massó, E. Seidel, and J. Stela, Phys. Rev. D **56**, 3405 (1997).

[10] M. Alcubierre, B. Brügmann, P. Diener, M. Koppitz, D. Pollney, E. Seidel, and R. Takahashi, Phys. Rev. D **67**, 084023 (2003).

[11] F. Pretorius, Classical Quantum Gravity **22**, 425 (2005).

[12] F. Pretorius, Phys. Rev. Lett. **95**, 121101 (2005).

[13] M. W. Choptuik, Phys. Rev. Lett. **70**, 9 (1993).

[14] C. Gundlach, Adv. Theor. Math. Phys. **2**, 1 (1998).

[15] C. Gundlach and J. M. Martín-García, Living Rev. Relativity **10**, 5(2007).

[16] E. Sorkin and M. W. Choptuik, Gen. Relativ. Gravit. **42**, 1239 (2010).

[17] J. D. Brown, Phys. Rev. D **79**, 104029 (2009).

[18] C. Gundlach, Phys. Rev. Lett. **75**, 3214 (1995).

[19] C. Gundlach, Phys. Rev. D **55**, 695 (1997).

[20] S. Hod and T. Piran, Phys. Rev. D **55**, R440 (1997).

[21] D. Garfinkle and G. C. Duncan, Phys. Rev. D **58**, 064024 (1998).

[22] J. M. Martín-García and C. Gundlach, Phys. Rev. D **59**, 064031 (1999).

[23] J. M. Martín-García and C. Gundlach, Phys. Rev. D **68**, 024011 (2003).

[24] F. Pretorius and M. W. Choptuik, Phys. Rev. D **62**, 124012 (2000).

[25] M. W. Choptuik, E. W. Hirschmann, S. L. Liebling, and F. Pretorius, Phys. Rev. D **68**, 044007 (2003).

[26] M. W. Choptuik, E. W. Hirschmann, S. L. Liebling, and F. Pretorius, Phys. Rev. Lett. **93**, 131101 (2004).

[27] A. Abrahams and C. Evans, Phys. Rev. Lett. **70**, 2980 (1993).

[28] M. Alcubierre, G. Allen, B. Brügmann, G. Lanfermann, E. Seidel, Wai-Mo Suen, and M. Tobias, Phys. Rev. D **61**, 041501 (2000).

[29] D. Garfinkle and G. C. Duncan, Phys. Rev. D **63**, 044011 (2001).

[30] O. Rinne, Classical Quantum Gravity **25**, 135009 (2008).

[31] E. Sorkin, Classical Quantum Gravity **28**, 025011 (2011).

[32] J. Healy and P. Laguna, Gen. Relativ. Gravit. **46**, 1722 (2014).

[33] L. S. Lara, M. Sc. thesis, Friedrich-Schiller-Universität Jena, 2006.

[34] D. Hilditch, T. W. Baumgarte, A. Weyhausen, T. Dietrich, B. Brügmann, P. J. Montero, and E. Müller, Phys. Rev. D **88**, 103009 (2013).

[35] M. Alcubierre, Phys. Rev. D **55**, 5981 (1997).

[36] M. Alcubierre, Classical Quantum Gravity **20**, 607 (2003).

[37] D. Garfinkle and C. Gundlach, Classical Quantum Gravity **16**, 4111 (1999).

[38] T. Baumgarte and S. Shapiro, *Numerical Relativity: Solving Einstein's Equations on the Computer* (Cambridge University Press, Cambridge, 2010).

[39] J. W. York, Jr., in *Sources of Gravitational Radiation*, edited by L. Smarr (Cambridge University Press, Seattle, 1979).

[40] M. Alcubierre and M. D. Mendez, Gen. Relativ. Gravit. **43**, 2769 (2011).

[41] A. Akbarian, FD: finite difference toolkit, http://laplace.phas.ubc.ca/People/arman/FD_doc (2014).

[42] J. Crank and P. Nicolson, Adv. Comput. Math. **6**, 207 (1996).

[43] M. Ruiz, M. Alcubierre, and D. Nunez, Gen. Relativ. Gravit. **40**, 159 (2008).

[44] I. Cordero-Carrión and P. Cerda-Duran, arXiv:1211.5930.

[45] P. J. Montero and I. Cordero-Carrión, Phys. Rev. D **85**, 124037 (2012).

[46] T. W. Baumgarte, P. J. Montero, I. Cordero-Carrión, and E. Müller, Phys. Rev. D **87**, 044026 (2013).

[47] H. Kreiss, H.-O. Kreiss, J. Oliger, (Global Atmospheric Research Programme and Joint Organizing Committee), in *Methods for the Approximate Solution of Time-Dependent Problems*, GARP publications series (International Council of Scientific Unions, World Meteorological Organization, 1973).